Spectrum-dependent image convolutional processing via a 2D polarization-sensitive photodetector

Zhongming Wei (✉ zmwei@semi.ac.cn)

Institute of Semiconductors, Chinese Academy of Sciences   https://orcid.org/0000-0002-6237-0993

Yali Yu

Institute of Semiconductors, Chinese Academy of Sciences

Tao Xiong

Institute of Semiconductors, Chinese Academy of Sciences

Ziqi Zhou

Institute of Semiconductors, Chinese Academy of Sciences

Duanyang Liu

Institute of Semiconductors, Chinese Academy of Sciences

Yue-Yang Liu

Institute of Semiconductors, Chinese Academy of Sciences

Juehan Yang

Institute of Semiconductors, Chinese Academy of Sciences

Article

Additional Declarations: (Not answered)

Spectrum-dependent image convolutional processing via a 2D polarization-sensitive photodetector

Yali Yu[1,2], Tao Xiong[1,2], Ziqi Zhou[1,2], Duanyang Liu[1], Yue-Yang Liu[1], Juehan Yang[1], Zhongming Wei[1,2,*]

[1]State Key Laboratory of Superlattices and Microstructures, Institute of Semiconductors, Chinese Academy of Sciences, Beijing 100083, China

[2]Center of Materials Science and Optoelectronic Engineering, University of Chinese Academy of Sciences, Beijing 100049, China

*Correspondence: zmwei@semi.ac.cn

Abstract

With the advancement of photodetectors and the widespread deployment of high-definition image sensors, the growth in processing capacity of traditional processors significantly lags behind the demands of real-time image processing. Consequently, achieving real-time image processing at the sensor level has emerged as a prominent research domain in the photodetector field, holding potential applications in various fields including remote sensing, autonomous driving, and road monitoring. This advancement underscores the need for photodetectors with enhanced multifunctional integration capabilities, capable of performing real-time computations on optical or electrical signals. In this study, we employ an innovative two-dimensional p-type semiconductor $GaTe_{0.5}Se_{0.5}$ as the light absorption layer to construct a photodetector with a polarization-sensitive wide-spectral photoresponse within the wavelength range of 255 to 1064 nm. This design enables the realization of a photodetector that integrates real-time sensing and computation. Leveraging the wide-spectral photoresponse of the photodetector, wide-spectral imaging was realized within the wavelength range of 390–810 nm during experimentation. Furthermore, by utilizing the tunable photoresponses of the photodetector through varying polarization angles, real-time image convolutional processing is enabled, aided by configuring appropriate convolution kernels based on the polarization-sensitive photoresponse values. Our proof-of-concept device, featuring spectrum-dependent polarization-sensitive photoresponses across a wide-spectral range, successfully accomplishes real-time image convolutional processing, including sharpness and edge extraction operations, thereby facilitating more precise capture of image details. The innovative design of the polarization-sensitive wide-spectral $GaTe_{0.5}Se_{0.5}$-based photodetector constitutes a notable contribution to the domain of real-time image perception and processing.

Keywords: p-type semiconductor, wide-spectral photoresponse, polarization-sensitive, convolutional processing

Introduction

Natural light is isotropic in all vibration directions, while polarized light exhibits anisotropy in different vibration directions. This anisotropy introduces a novel dimension to the information carried by light, offering substantial potential applications in the transmission, acquisition, and analysis of optical information[1, 2, 3, 4]. Examples include material structure anisotropy assessment[5, 6, 7], optical anisotropy analysis of objects[8, 9, 10, 11], enhancement of data transmission bandwidth and security[12, 13]. These applications find significant advantages in various fields such as material characterization, polarization imaging, optical communication, and remote sensing[14, 15, 16, 17]. Traditional photodetectors struggle to discern the variations in polarized light across different vibration directions. To harness the aforementioned advantages of polarized light, a specialized design of polarized photodetectors is required in the field of optoelectronic imaging[18, 19]. Among various types of polarization detectors, polarization-sensitive photodetectors constructed from anisotropic two-dimensional (2D) semiconductors offer high sensitivity for polarized photodetection[17]. Additionally, they possess the benefits of low power consumption, compact size, and high integration without the need for a preceding polarizing grating structure[20]. These advantages allow for adaptation to diverse application scenarios, greatly expanding their scope of application.

With the advancement of photodetector technology and the widespread deployment of high-definition image sensors, the growth of traditional processors' processing capacity has significantly lagged behind the real-time processing demands of images[21]. As a result, achieving real-time image processing at the sensor end has emerged as a focal point in the field of photodetectors[22]. In order to integrate both the perception and processing of optical signals within the sensor itself, specialized optoelectronic devices with distinct properties are often employed to implement common image processing techniques such as convolution operations[21, 23, 24]. These optoelectronic devices typically possess modulatable optoelectronic characteristics, enabling them to exhibit adjustable photoresponses to the specific incident light, thereby facilitating real-time processing while sensing optical signals[25]. Currently, a prevalent approach for

modulating the photoresponse of the device involves adjusting the gate voltage[21, 25, 26]. Considering the diverse variety, high mobility, and tunable bandgap of emerging 2D semiconductors, photodetectors constructed from these semiconductors often exhibit multifunctional capabilities[27, 28, 29]. In this paper, we present an innovative method that utilizes the polarization-sensitive photoresponse of the photodetector for image convolutional processing. Beginning with the active light absorption selection for the polarization-sensitive photodetector, our work involves the fabrication of a 2D semiconductor $GaTe_{0.5}Se_{0.5}$ with anisotropic wide-spectral photoresponse. A comprehensive analysis of its fundamental characteristics, including crystal structure, thermal stability, and anisotropic light absorption, is conducted through a combined approach of theoretical predictions and experimental validations. With a solid understanding of the basic properties of $GaTe_{0.5}Se_{0.5}$, we proceed to construct a polarization-sensitive photodetector by incorporating it as an active light absorption layer. A thorough testing and analysis of its photoresponse and polarization-sensitive characteristics are conducted, revealing that the device exhibits a wide-spectral photoresponse across the entire ultraviolet-visible-near-infrared spectrum (UV-Vis-NIR, 255-1064 nm) and demonstrates distinct polarization-sensitive capabilities within the range. Leveraging the polarization-sensitive photoresponse of the device, the convolution kernels are configured based on the output polarization-sensitive photocurrent values, enabling synchronous image convolution operations, including sharpness and edge extraction. This approach provides great promise for scaling down the footprints of polarization-sensitive photodetectors to the micrometer scale, making substantial contributions to the integration of optical signal real-time perception and processing within the sensor.

Results

The mechanism for achieving image convolutional processing using a polarization-sensitive 2D semiconductor-based photodetector relies on the modulation of polarization-sensitive photoresponses through the control of polarization angles. In order to realize image convolutional processing, it is crucial for the device to exhibit remarkable polarization-sensitive characteristics and for these attributes to be utilized in configuring appropriate convolution kernels. Based on the aforementioned analysis, the photodetector constructed from the 2D semiconductor $GaSe_{0.5}Te_{0.5}$, possessing wide spectral responsivity and polarization-sensitive properties, demonstrates significant potential for applications. The operational mechanism of convolutional processing is depicted in Fig. 1a, wherein a polarization pathway is integrated with appropriate polarization-sensitive photocurrents to configure convolution kernels, thereby enabling the sharpness and edge extraction of images perceived by the device. Hence, the quest for high-performance and reliable semiconductors to construct functionally enriched photodetectors is significant in the context of this work. As illustrated in Fig. 1b, Ab initio molecular dynamics (AIMD)[30, 31] can be employed to simulate and verify the thermal stability of the monolayer semiconductor $GaSe_{0.5}Te_{0.5}$. This includes the equilibrium atomic structure diagram of $GaSe_{0.5}Te_{0.5}$ before and after heating for 3 ps, as well as the time-dependent evolution of $GaSe_{0.5}Te_{0.5}$ simulated via AIMD at 300 K. The results allow for the analysis that, under the temperature conditions of 300 K and a heating duration of 3 ps, the atomic structure of $GaSe_{0.5}Te_{0.5}$ remains robust, exhibiting only slight deformation. Furthermore, at room temperature, neither structural reconfiguration nor bond rupture occurs within $GaSe_{0.5}Te_{0.5}$, confirming its thermal stability at room temperature conditions. The thermal stability characteristic of $GaSe_{0.5}Te_{0.5}$ provides a reliable assurance for the application demonstration in this work and has stimulated our interest in further exploring its other properties. As a theoretical foundation for exploring semiconductor properties, the electronic band structure and the magnitude of the bandgap width are crucial. Density functional theory (DFT)[32, 33, 34] was applied to investigate the electronic and optical properties. The atomic arrangements in different planes were shown in Fig. S1, and crystal constants used for

theoretical prediction were a=3.97 Å, b=3.97 Å, and c=16.54 Å. As depicted in Fig. 1c, monolayer $GaSe_{0.5}Te_{0.5}$ is demonstrated as a direct bandgap semiconductor with a bandgap width of approximately 1.91 eV through the integral path of the band structure is $\Gamma \rightarrow M \rightarrow K \rightarrow \Gamma$. Bulk $GaSe_{0.5}Te_{0.5}$ is demonstrated as a direct bandgap semiconductor as well with a bandgap width of approximately 1.06 eV (shown in Fig. S2). Projected density of states (PDOS)[35], as an effective methodology, can be employed to investigate the electronic contributions of the three elements, Ga, Te, and Se. As depicted in Fig. 1d, the energy levels associated with Te exhibit a propensity to occupy higher energy states compared to Se. Consequently, the substantial incorporation of Te, in contrast to GaSe, notably diminishes the material's bandgap width, thus effectively broadening the material's optical absorption range. This deduction is in alignment with prior reports[36, 37]. Furthermore, an analysis of the anisotropic optical absorption properties along the a- and b- axes of the $GaSe_{0.5}Te_{0.5}$ crystal is presented in Fig. 1e. Over the wavelength range of 200-800 nm, the monolayer $GaSe_{0.5}Te_{0.5}$ demonstrates characteristics of anisotropic light absorption. A significant discrepancy emerges within the wavelength range of 200-500 nm, a trait that substantiates the robust foundation for constructing polarization-sensitive photodetectors based on $GaSe_{0.5}Te_{0.5}$ in subsequent investigations. Fig. 1f and 1g respectively illustrate the partial charge densities (PCDs) of the conduction band minimum (CBM) and valence band maximum (VBM) within the b-c and a-c planes. The spatial structures of the wave functions for CBM and VBM align with the analysis of the PDOS. Significant differences exist in the spatial distribution of wave functions for CBM and VBM along the a- and b- axes. This further clarifies the anisotropic characteristic in both the monolayer and bulk $GaSe_{0.5}Te_{0.5}$ (Fig. S3).
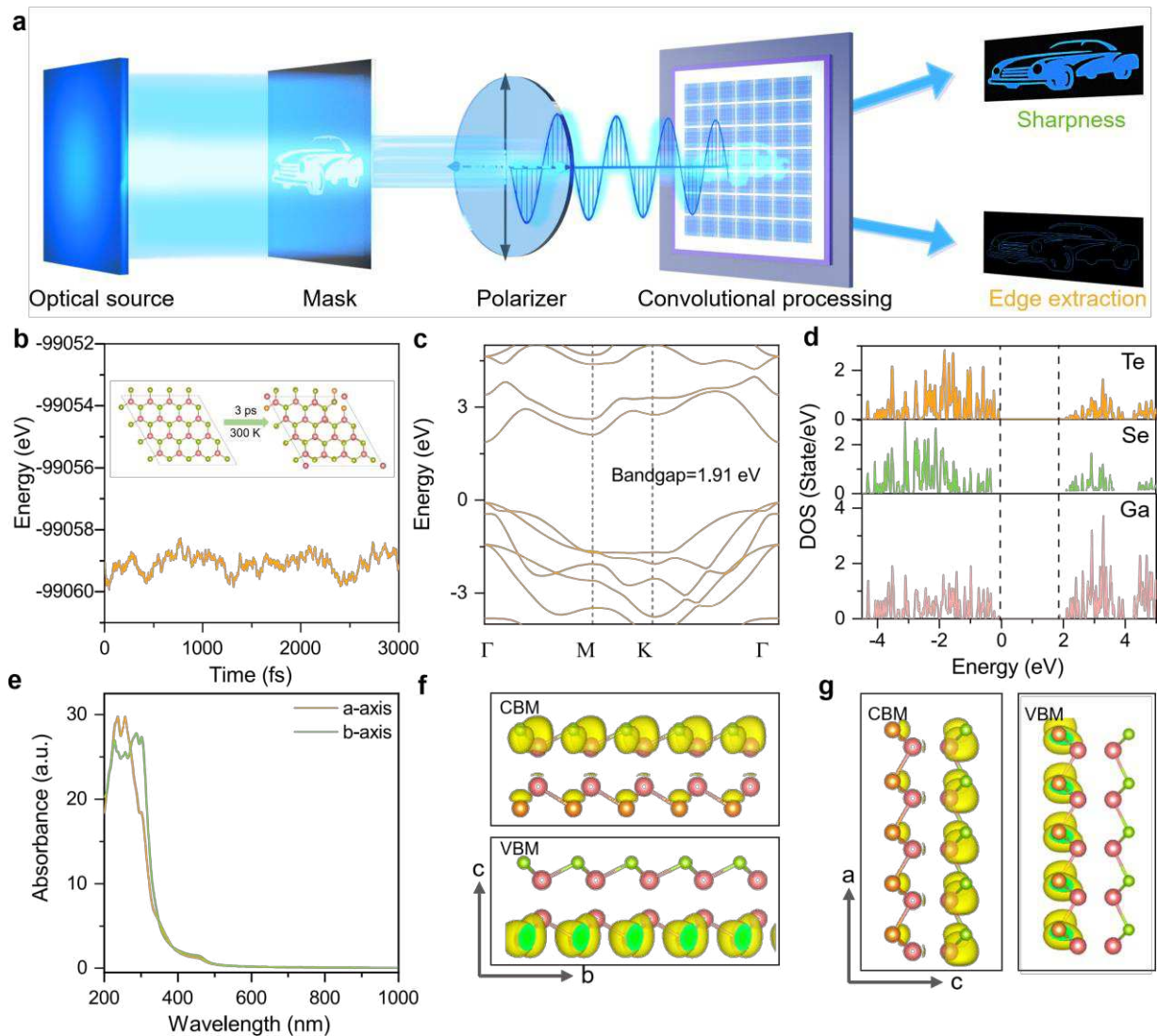
Fig. 1 Convolutional processing mechanism and material design. a Schematic of convolutional processing based on a polarization-sensitive photodetector fabricated using 2D GaSe$_{0.5}$Te$_{0.5}$ semiconductor. **b** Energy profile of GaSe$_{0.5}$Te$_{0.5}$ as a function of Ab initio molecular dynamics (AIMD) time at 300 K. Insets depict AIMD snapshots of GaSe$_{0.5}$Te$_{0.5}$ before and after heating. **c** Electronic band structure of monolayer GaTe$_{0.5}$Se$_{0.5}$. **d** Local projected density of states (PDOS) of GaTe$_{0.5}$Se$_{0.5}$. **e** Calculated absorbance coefficient along the a-axis and b-axis for bulk GaTe$_{0.5}$Se$_{0.5}$. **f** Iso-plots of the charge density distribution of GaTe$_{0.5}$Se$_{0.5}$ at the CBM and VBM states within the b-c plane, respectively. **g** Iso-plots of the charge density distribution of GaTe$_{0.5}$Se$_{0.5}$ at the CBM and VBM states within the a-c plane, respectively.

The innovative semiconductor GaTe$_{0.5}$Se$_{0.5}$ was synthesized using the chemical vapor

transport (CVT) method (see Methods section for growing details). To investigate the crystal structure and composition of $GaTe_{0.5}Se_{0.5}$, high-resolution scanning transmission electron microscopy (STEM) was employed. Fig. 2a shows the high-resolution cross-sectional STEM image of $GaTe_{0.5}Se_{0.5}$, displaying a distinctive layered structure in an "ABAB" stacking arrangement, with a measured interlayer spacing of 8.11 Å. This conclusion aligns with the atomic arrangement along the crystal a-c plane shown in Fig. 2c. Additionally, the measured interlayer spacing corresponds to half the value of the c-axis (c=16.54 Å) of the unit cell, confirming the hexagonal lattice structure as a 2H phase. Complementary, combined with the energy dispersive spectrometry (EDS) data as shown in Fig. 2b, a coherent positioning of Se and Te atoms within the structure was revealed, forming bonds with Ga atoms. The approximate 1:1 ratio between Se and Te atoms further confirms their comparable occupancy in the lattice. Consequently, these findings collectively validate the elemental composition of Ga, Te, and Se within the crystal, with an approximate ratio of 2:1:1. In order to further validate the crystal orientation and chemical bond vibration symmetry of the $GaTe_{0.5}Se_{0.5}$, Raman spectroscopy was employed under the excitation of a 532 nm laser, as depicted in Fig. 2d. Furthermore, the anisotropy inherent to $GaTe_{0.5}Se_{0.5}$ was systematically explored through orientation-dependent polarized Raman spectroscopy. The assignment of peaks related to the A_g (out-of-plane) and E_g (in-plane) vibrational modes was guided by previous Raman analyses conducted on GaTe[37] and GaSe[38]. In the unpolarized measurement configuration, the Raman spectrum of $GaTe_{0.5}Se_{0.5}$ shows three distinct peaks located at 126, 224, and 301 cm^{-1}, respectively. The positions of these three peaks align closely with reported in prior literature[36]. The assigned modes correspond to $A_g^{(1)}$, E_g, and $A_g^{(2)}$ modes, providing an additional confirmation of the material's classification as the 2H phase. By introducing polarization optics into the detection pathway and operating in both parallel and vertical modes, variations in the intensity and peak positions become evident, underscoring the sensitivity of the Raman response to different polarization states. In Fig. 2e, photoluminescence (PL) characterization was employed to evaluate the crystalline quality of the synthesized $GaTe_{0.5}Se_{0.5}$ compound and to further explore its electronic structure and bandgap width.

Through the utilization of a 532 nm laser excitation, an obvious photoluminescence peak shown around 1.7 eV, unaccompanied by conspicuous ancillary features, which is also consist with the previous reported[36]. This particular observation lends credence to the notion that $GaTe_{0.5}Se_{0.5}$ manifests a notably high degree of crystalline integrity, indicative of a typical direct bandgap semiconductor. The deduced approximate value for the bandgap width is approximately 1.7 eV. By comparing the conclusions drawn from Fig. 1c and Fig. S2, it can be inferred that the $GaTe_{0.5}Se_{0.5}$ nanosheets used in the experiment possess a few-layer structure. Absorption spectrum was conducted to verify the bandgap width of $GaTe_{0.5}Se_{0.5}$. By employing the established relationship: $E_g = 1240/\lambda\ (nm)$, it was deduced from the absorption spectrum that the material's absorption onset occurs at approximately 750 nm (Fig. 2f). Consequently, the calculated bandgap width E_g aligns remarkably well with the conclusion drawn from the PL assessment. Second harmonic generation (SHG) stands as a paradigmatic nonlinear optical phenomenon, offering discernment into the structural attributes and properties of materials through their non-linear optical response[39, 40]. In this work, the second-order nonlinear optical response of $GaTe_{0.5}Se_{0.5}$ was systematically assessed. Employing an excitation wavelength of 1064 nm laser, the outcome of this inquiry is illustrated in Fig. 2g. The obvious emission signal detected at half the excitation wavelength, namely at 532 nm, definitely confirms the occurrence of the second-order nonlinear optical effect. Relevantly, the observed SHG emission signal intensity exhibited incremental augmentation as the pump power, increased from 7 to 32 mW. Notably, during this processing, the spectral position of the emission signal remained invariant. Through an empirical analysis involving data extracted from Fig. 2g, a notably slope of approximately 1.79 emerged in the relationship linking the pump power and the SHG intensity is shown in Fig. 2h. This proximity to the theoretical value of 2 distinctly accentuates the quadratic dependence of SHG intensity on pump power, consistent with the prediction of the electric-dipole theory. This underlying consistency highlights the congruence with the prediction that, under first-order perturbations, the SHG intensity is directly proportional to the square of the laser power[39]. Fig. 2i illustrates a polar plot of polarization-resolved SHG spectra in the parallel configuration.

The depicted signal exhibits pronounced azimuthal dependence, suggesting a robust manifestation of directional sensitivity within the SHG response. This notable anisotropy is consistent with the intricate crystalline structure of $GaTe_{0.5}Se_{0.5}$, thereby yielding credible insights into its distinctive anisotropic characteristics. In essence, similar to the behavior exhibited by H-GaTe[41], this observation is notably consistent with the predicted anisotropy stemming from the crystallographic traits of $GaTe_{0.5}Se_{0.5}$.
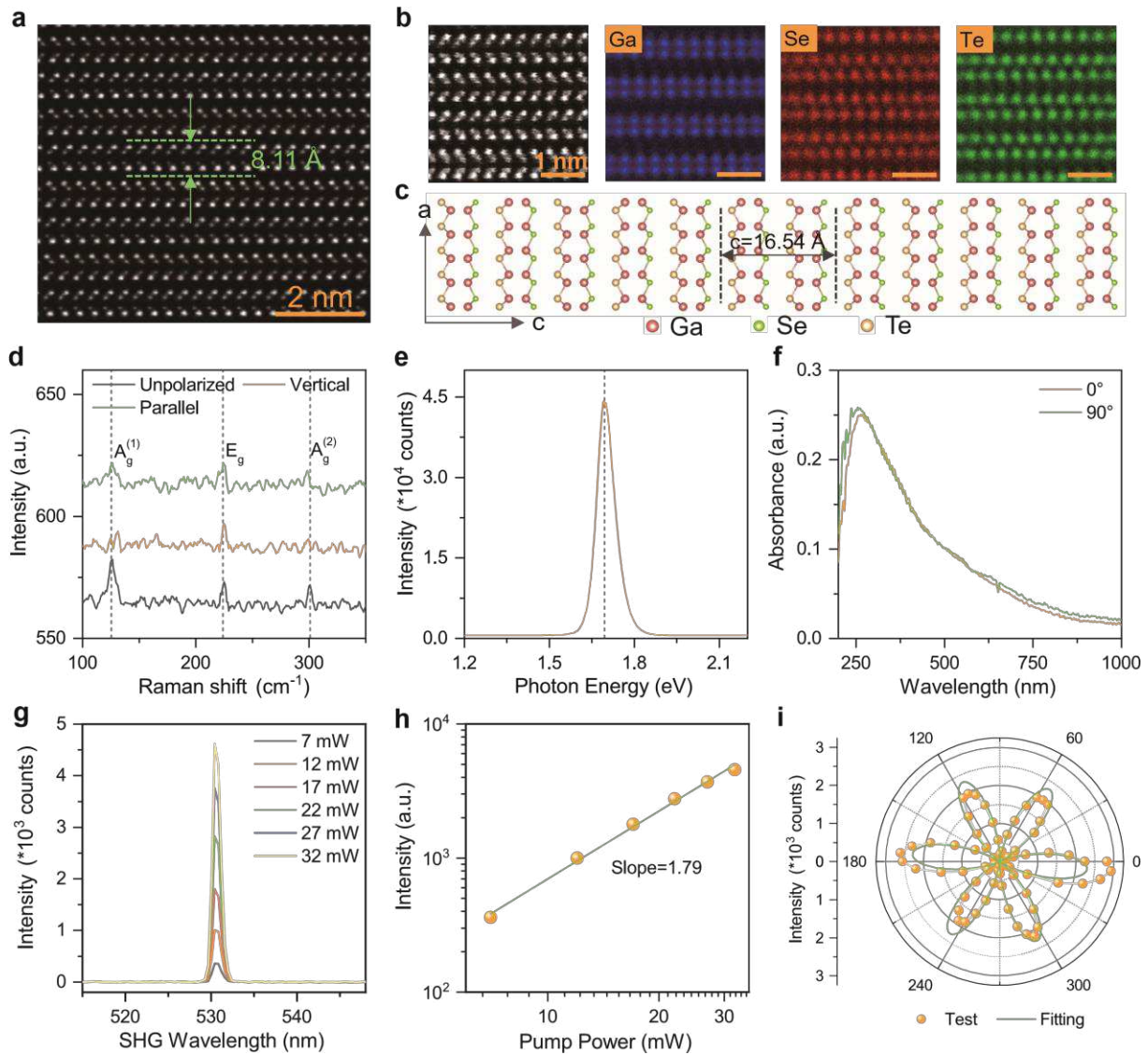

Fig. 2 Characterization of Materials. a High-resolution cross-sectional STEM image revealing hexagonal layered atomic arrangement. **b** Atomically resolved EDS elemental mapping images depicting the distribution of Ga, Se, and Te. **c** View of the atomic model of $GaTe_{0.5}Se_{0.5}$ within the a-c plane. **d** Raman spectra obtained in both unpolarized and polarized (parallel and vertical modes) configurations. **e** PL spectrum

of $GaTe_{0.5}Se_{0.5}$. **f** Absorption spectra acquired at polarization angles of 0° and 90°. **g** SHG spectra measured under various pump power, with an excitation laser wavelength of 1064 nm. **h** Typical pump power-law dependence of SHG intensity with a fitted coefficient of 1.79. **i** Polarization-resolved SHG spectra along the parallel direction, revealing distinctive sixfold rotational symmetry.

An UVC-Vis-NIR photodetector with a wide-spectral photoresponse was constructed based on $GaTe_{0.5}Se_{0.5}$. The construction processing involved the preparation of multi-layered $GaTe_{0.5}Se_{0.5}$ through mechanical exfoliation method, followed by a dry transfer onto a Si substrate with a 300 nm SiO_2 layer serving as the dielectric layer. The Si substrate was employed as the back gate for the field-effect transistor (FET), as illustrated in Fig. 3a (further details on fabrication can be found in the Methods section). During the experimental processing, the device's transfer characteristics were evaluated by applying a range of gate voltages from -40 to 40 V on the gate electrode while maintaining a 2 V drain-source voltage. The results, depicted in Fig. 3b, revealed the distinctive p-type transfer characteristics of the $GaTe_{0.5}Se_{0.5}$-based FET, confirming $GaTe_{0.5}Se_{0.5}$ as a novel p-type semiconductor. A comparative analysis of the photoresponse spectral with other typical p-type semiconductor, as shown in Fig. 3c[42, 43, 44, 45, 46, 47, 48, 49], highlighted the broader spectral coverage of $GaTe_{0.5}Se_{0.5}$. The device's photoresponse spectrum spanned 255–1064 nm, encompassing the entire spectrum from UVC to NIR. Thus, $GaTe_{0.5}Se_{0.5}$ semiconductor presents itself as suitable for constructing phototransistors with both wide-spectral photoresponse characteristics and p-type transfer properties. In order to further explore additional photoelectrical properties of the $GaTe_{0.5}Se_{0.5}$-based photodetector, involving wavelength-dependent I-V and I-t curves within the range of 255–1064 nm was conducted in the experiment. As shown in Fig. 3d, the current output of the device under constant power density illumination at different wavelengths within the bias range of -1.5 to 1.5 V was presented. Analysis of the data reveals that the device exhibits maximum output current under 255 and 360 nm laser irradiation. Subsequently, with increasing incident laser wavelength, the photocurrent gradually decreases. At the illumination laser wavelength

of 1064 nm, the photocurrent becomes exceedingly weak compared to the dark current, with a photo-to-dark current ratio close to 1.5 (Fig. S4). In the photo-to-dark switching test illustrated in Fig. 3e, the output photocurrent values by the device under different wavelength laser irradiation, while maintaining a constant incident laser power density, mirror the same trend as in Fig. 3d. Moreover, following 10 cycles of light-switching stability testing, the device exhibited consistent and stable characteristics under various laser irradiation wavelengths, thereby providing a robust foundation for subsequent imaging applications. Two fundamental parameters, responsivity (R) and detectivity (D*), served as key indicators of photodetector performance, and were subject to testing and analysis in this study. The calculation methods are presented in Equations (1) and (2), as illustrated below:

$$R = \frac{I - I_{dark}}{P \times S} \tag{1}$$

$$D^* = \frac{R\sqrt{S}}{\sqrt{2eI_{dark}}} \tag{2}$$

Where I and I$_{dark}$ represent the output current and dark current, respectively; P is the power density of the illumination laser; and S indicates the effective area of the device. As depicted in Fig. 3f and Table S1, the device demonstrated the highest R under 360 nm laser irradiation, reaching a value of 0.164 A/W, with a detectivity of 0.37×10^9 Jones. Furthermore, the values of R and D* under 255 nm laser irradiation closely approximated the values got in 360 nm, indicating the excellent photoresponse capability of the device across the entire UV range covering UVC to UVA. While the device's photoresponse capability in the Vis and NIR wavelength ranges may not be as exceptional as that in the UV range, it is operational across the 255–1064 nm spectrum. The investigation of the power dependence of the device under different incident laser irradiations was also conducted in this study, and the results are depicted in Fig. 3g and 3h. When the device was exposed to 255 nm laser irradiation, the output photocurrent demonstrated an obvious reduction as the incident laser power sequentially decreased from 35 to 3 mW/cm^2, highlighting a robust power-dependent behavior of the output photocurrent. To further explore the potential linear intensity dependence of the photocurrent, Fig. 3h illustrates the photocurrent values obtained as the incident light

power density varies under laser irradiation at wavelengths of 255, 520, and 1064 nm. Utilizing the equation (3) for fitting purposes:

$$I = \alpha \times P^{\beta} \tag{3}$$

where I is the photocurrent, P represents the incident light power density, α denotes the proportionality constant, and β represents the fitting parameter. The fitted results yielded β values of 0.74, 0.81, and 1.03 for wavelengths of 255, 520, and 1064 nm, respectively, illustrating that the extracted values for β are closely aligned with 1 across the spectrum of wavelengths used in the experiment. This exceptional linear correspondence between light intensity and photocurrent ensures the acquisition of high-quality imaging[21]. Furthermore, the photoresponse speed of the $GaTe_{0.5}Se_{0.5}$-based photodetector, another vital parameter influencing imaging applications, is discussed in Fig. 3i. Under 450 nm wavelength laser illumination, both rise time and fall time are on the microsecond scale, indicative of fast photoresponse speed, thereby assuring the feasibility of the device in imaging applications.
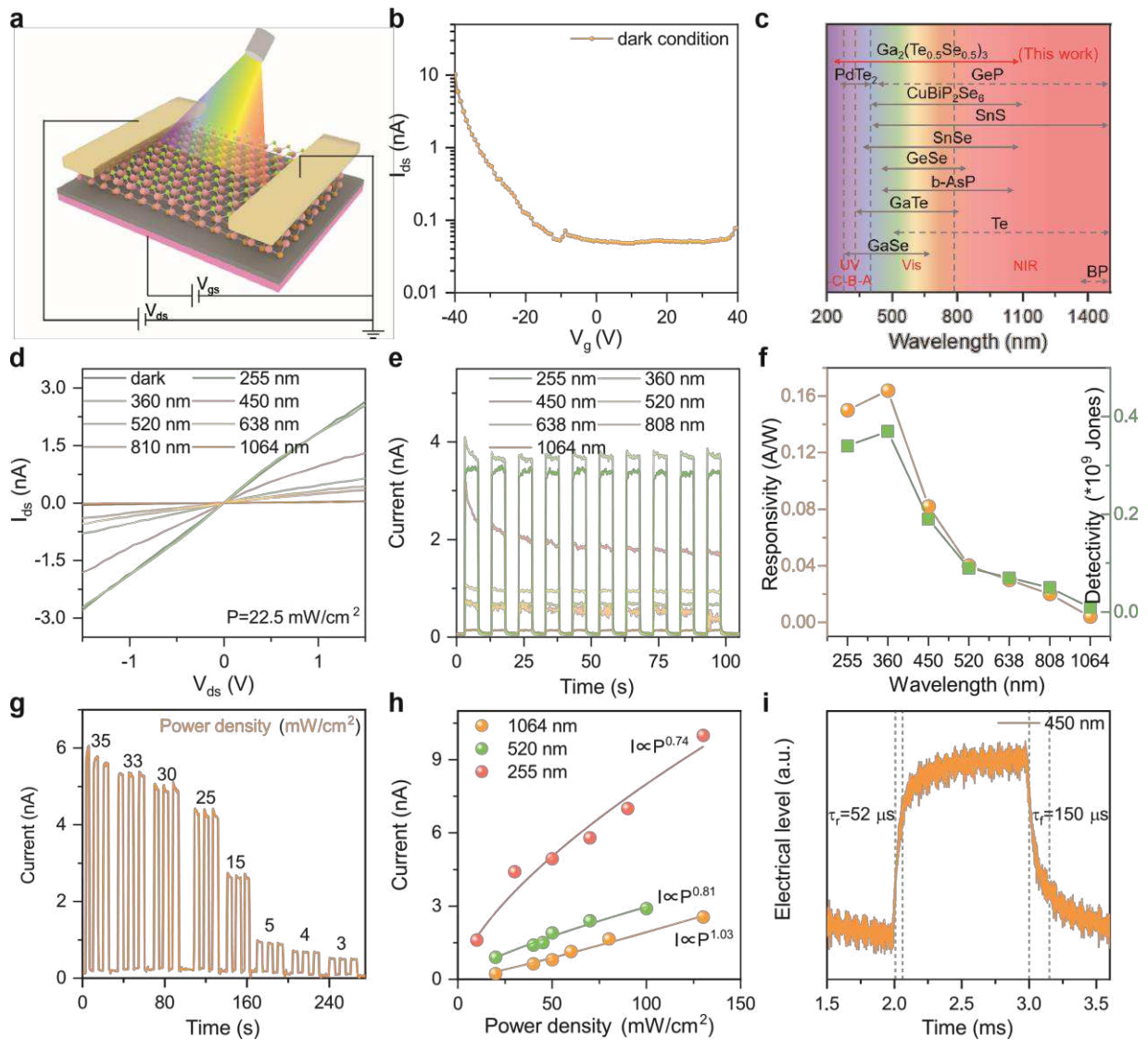
Fig. 3 Device performance characterization. a Schematic representation of the GaTe$_{0.5}$Se$_{0.5}$-based field-effect transistor (FET), utilizing a Si substrate as the back gate. **b** Transfer characteristic curve of the GaTe$_{0.5}$Se$_{0.5}$-based FET under V$_{ds}$ = 2 V. **c** Comparison of the photoresponse spectral range of FET fabricated through p-type semiconductors, demonstrating the wide-spectral photoresponse capabilities of GaTe$_{0.5}$Se$_{0.5}$ covering the UV-Vis-NIR regions. **d** Wavelength-dependent I$_{ds}$-V$_{ds}$ curves tested under a consistent illumination power density. **e** Investigation of GaTe$_{0.5}$Se$_{0.5}$-based device stability through 10 cycles of photo-to-dark switching under incident light of varying wavelengths. **f** Responsivity and detectivity of the device across the spectral range of 255–1064 nm. **g** Power-dependent output current at the illumination wavelength of 255 nm. **h** Characterization of the photocurrent in relation to power

density under incident wavelengths of 255, 520, and 1064 nm, respectivly. **i** Photoresponse speed (rise and fall times) of the device, highlighting its rapid optically-induced switching behavior within the microsecond timeframe.

The results of both theoretical predictions and experimental absorption revealed the anisotropic characteristics of the $GaTe_{0.5}Se_{0.5}$, prompting us to delve deeper into the investigation of the polarization-sensitive photoresponse within the $GaTe_{0.5}Se_{0.5}$-based photodetector. In the processing of experimentation, a Glan-Taylor prism was introduced into the optical path between the photodetector and the incident laser to convert the incident light into linearly polarized light. Subsequently, a half-wave plate was further introduced into the optical path to manipulate the angle of linearly polarized light. At this stage, the optical setup required for evaluating the polarization-sensitive characteristics of the device was established. The operational mechanism of the polarization-sensitive photoresponse can be illustrated through polarized photocurrent mapping under 450 nm laser illumination. The dashed boxes in Fig. 4a-4c delineate the locations of the source, drain, channel, and the active light-absorbing region, where the $GaTe_{0.5}Se_{0.5}$ is situated. Operated under a gate voltage of 0 V and a source-drain voltage of 1 V, the device underwent photocurrent scanning across the selected regions as depicted. The results revealed the generation of photocurrent at the junction of the drain and $GaTe_{0.5}Se_{0.5}$, which confirmed the presence of a Schottky barrier between the metal and the semiconductor, allowing photo-generated carriers to surmount the barrier and flow to the drain, thus accounting for the generation of photocurrent. Under polarization angles of 0°, 45°, and 90°, the photocurrent values produced by the device exhibited a progressive decrease. This trend signifies the polarization-sensitive characteristic of the $GaTe_{0.5}Se_{0.5}$-based photodetector. The polarization sensitivity of the $GaTe_{0.5}Se_{0.5}$-based photodetector at additional wavelengths was also investigated, and the results are depicted in Fig. 4d-4f. Under laser illuminations at wavelengths of 255, 520, and 1064 nm, and at a source-drain voltage of 2 V, angle-dependent photocurrent values were depicted in polar coordinate plots. From the illustrations, it is discernible that, upon fitting the output anisotropic photocurrents, the device exhibits noticeable polarization

sensitivity across the entire spectrum from UVC to NIR within the 0°-360° range. The ratios of anisotropic photocurrent magnitudes were quantified as 1.06, 1.15, and 1.32, respectively.
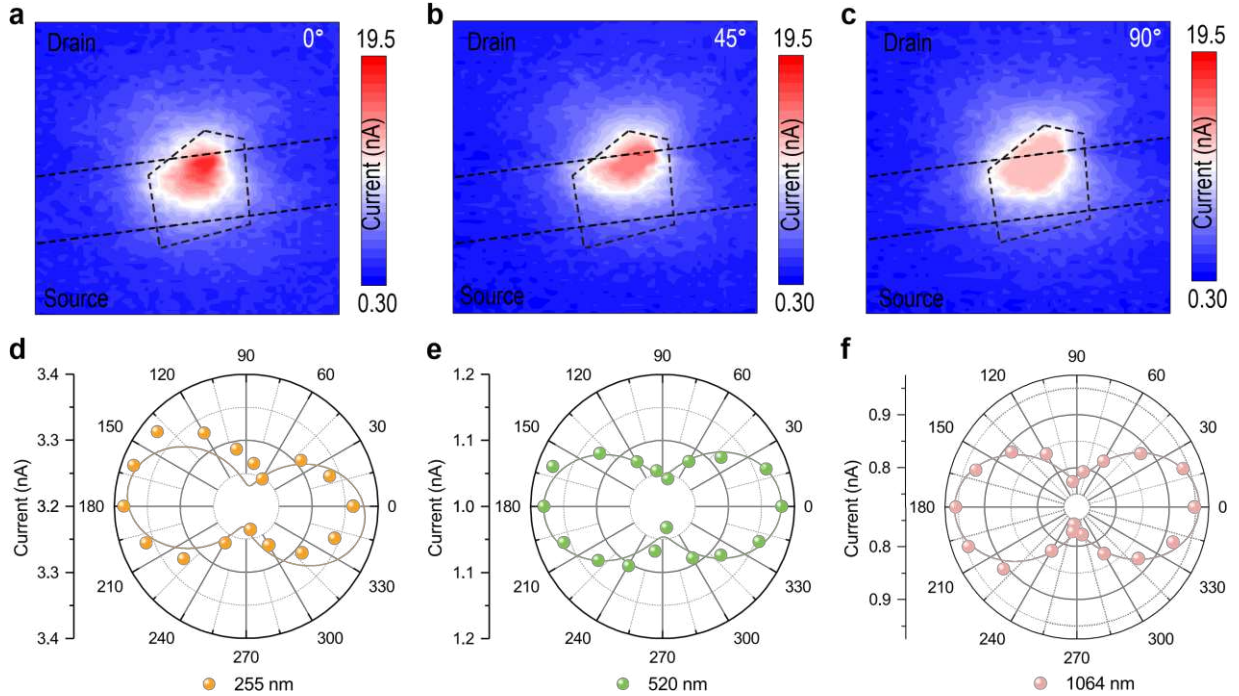

Fig. 4 Polarization-sensitive performance. a-c Photocurrent mappings were generated by scanning the GaTe$_{0.5}$Se$_{0.5}$-based photodetector under 450 nm laser illumination, while systematically varying the polarization angle from 0°, 45°, to 90°. Polarization-sensitive photoresponse was captured under **d** 255 nm laser illumination, **e** 520 nm laser illumination, **f** 1064 nm laser illumination, with the polarization angle being systematically adjusted from 0° to 360°.

Benefiting from the excellent wide-spectral UV-Vis-NIR photoresponse ability and fast photoresponse speed illustrated in Fig. 3, and the outstanding polarization-sensitive photoresponse properties demonstrated in Fig. 4, the application potential of the GaTe$_{0.5}$Se$_{0.5}$-based image sensor in the domain of wide-spectral imaging was further investigated, along with its utilization for image convolution processing involving sharpness and edge extraction, capitalizing on its polarization-sensitive properties. In the realm of wide-spectral imaging, a comprehensive optical scanning system capable of simultaneous recognition in three distinct spectral bands was established during the experimental procedure. The specific components and optical pathways of the system

are delineated in Fig. 5a. The sensor's capability for two-dimensional motion was harnessed through precise control of the stepper, facilitating point-to-point scanning of the imaging subjects. Simultaneously, incident light with specific patterns at varying wavelengths was effectively converged by incorporating suitable beamsplitters into the optical pathways. The final scanned grayscale image was subsequently transmitted to the computer system for analysis. Through the application of false-colored processing, a series of images corresponding to distinct objects, namely "monocycle" (responsive to 254 nm light), "truck" (responsive to 390 nm light), "bus" (responsive to 520 nm light), and "car" (responsive to 810 nm light), are depicted in Fig. 5b. Due to the incapability of the lens to effectively penetrate 254 nm light, the utilization of the lens for focusing purposes was omitted during the imaging procedure, yielding a blurred depiction of the image's contours. The results of the imaging endeavor serve to underscore the wide-spectral photosensitive attributes of the $GaTe_{0.5}Se_{0.5}$ unit within the image sensor, establishing its potential application in the domain of wide-spectral imaging across the UV–Vis–NIR spectral range. As a typical representative of the hyperspectral image, in order to further validate the potential application of the image sensor in the realm of remote sensing for wide-spectral detection, an additional experimental demonstration was conducted involving the utilization of three distinct landscape categories: soil, river, and tree. The purpose of this demonstration was to exhibit the viability of three-bands hybrid imaging. Employing the image-capturing setup, false-colored grayscale images were also procured. As illustrated in Fig. 5c, the presented composite image encompasses the "soil" (responsive to 390 nm light), "tree" (responsive to 520 nm light), and "river" (responsive to 810 nm light) representations. Owing to the precision constraints of the imaging equipment, the initial letters of the terms "soil," "river," and "tree" were selected to symbolize the corresponding objects within the process of three-bands hybrid imaging. This empirical evidence underscores the substantiated capacity of the photosensitive $GaTe_{0.5}Se_{0.5}$ unit to perform effectively in the context of multi-bands imaging, particularly within the context of remote sensing applications. Noise power spectrum, serving as another pivotal factor impacting image quality, was examined under specific conditions: source-drain voltage of 1 V, gate

voltage of 0 V, and the testing environment maintained in a dark state, as depicted in Fig. 5d. Through fitting via Equation (4),

$$S = S_0 \frac{I^\beta}{f^\alpha} \qquad\qquad (4)$$

wherein S represents noise power density, I represents the device's current value, S_0 is a bias-dependent constant, and α and β are fitting parameters. A comprehensive analysis was conducted and the obtained value of the fitting parameter α is 0.99, which closely approximates 1. Consequently, this result confirms that the device is dominantly subject to 1/f noise at low frequencies, a type of noise originating from the fluctuation of transport carriers. This conclusion further underscores the reliability of our imaging results. Fig. 5e illustrates the polarization-sensitive photoresponses of the device within the wavelength range of 400–850 nm, where polarization data was collected at intervals of 30°. It can be observed that the device's anisotropic photocurrent is maximized at polarization angles of 0° and 180°, with the two photoresponse curves nearly overlapping. Conversely, the anisotropic photocurrent is minimized at a polarization angle of 90°. This conclusion aligns with the findings in Fig. 4, further corroborating the device's consistent polarization-sensitive characteristics across the entire spectral range. This validation underscores the device's potential for reliable utilization in image convolution processing via its polarization-sensitive properties, offering robust data support for such applications. Convolution is a mathematical operation that involves element-wise multiplication and summation of a convolution kernel with the pixels of an existing image. By assigning specific weights to the values of the convolution kernel, it can be applied for various image processing tasks, such as smoothing, sharpness, edge enhancement, and edge extraction. In this work, as a proof of concept, convolution operations were performed by sequentially receiving each pixel of the image using a single device. Utilizing the anisotropic photocurrent values generated by the device at 450 nm (shown in Fig. S5 and Table S2), appropriate convolution kernels were configured to achieve image sharpness and edge extraction tasks. As illustrated in Fig. 5f, we designed a 5×5 convolution kernel. By comparing the resulting image with the original image obtained from imaging, significant sharpening effects were achieved by

element-wise multiplication and summation of the device's output polarized photocurrents at polarization angles of 90° and 0° with the original image's pixels. Furthermore, employing the device's output polarized photocurrents at polarization angles of 75° and 0° as convolution kernels and applying the same element-wise multiplication and summation process, significant edge extraction effects were attained in the resulting image. Under these conditions, the traditional convolution kernels for image sharpness and edge extraction were used for comparison. The obtained effects align closely with the fundamental outcomes of our proposed approach utilizing anisotropic photocurrent values for image convolution operations. Thus, this demonstration substantiates the feasibility of our innovative method proposed in this study.
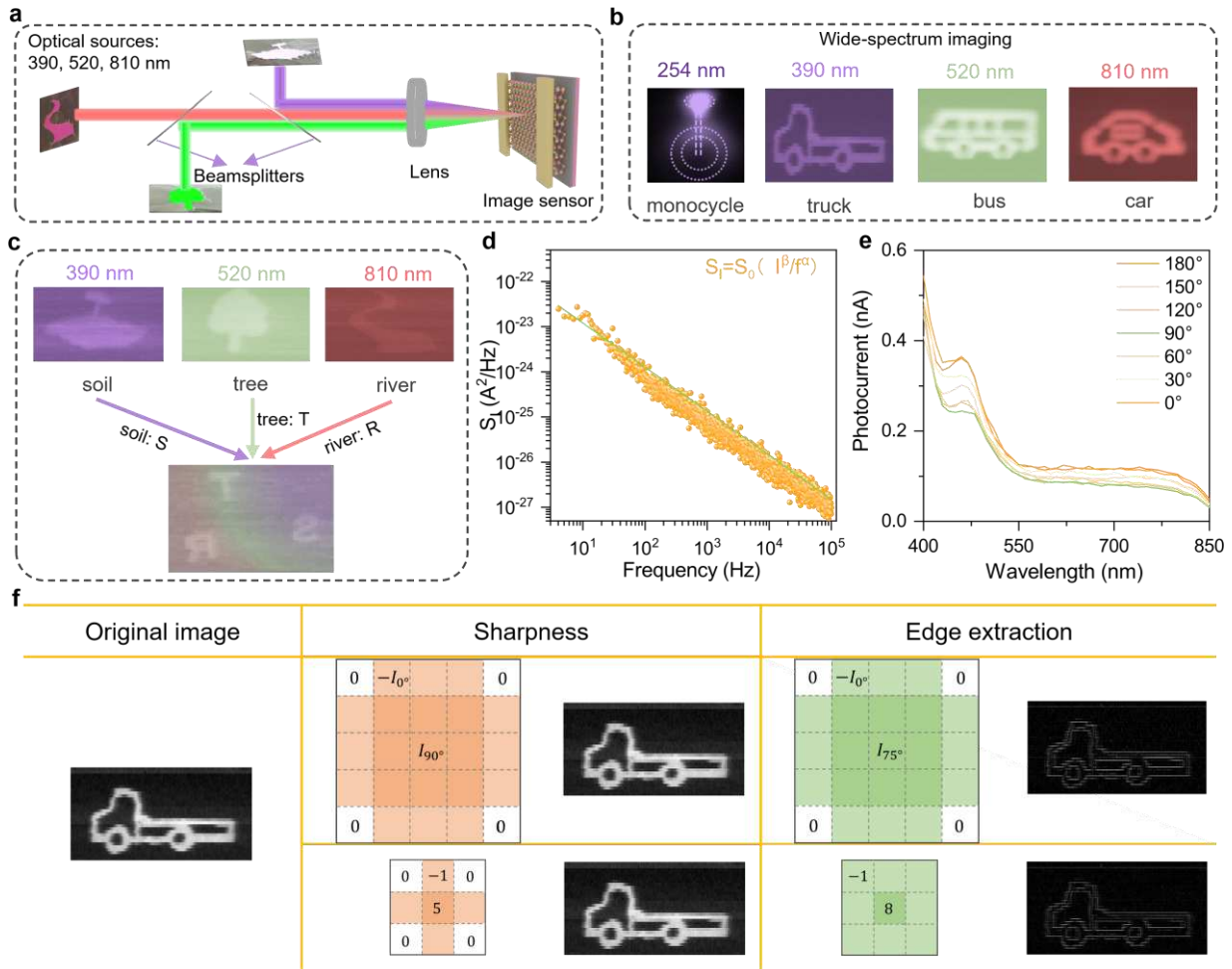

Fig. 5 Wide-spectral imaging and convolutional processing. a Schematic optical path arrangement of the image scanning system. **b** Scanned grayscale images of "monocycle" (254 nm), "truck" (390 nm), "bus" (520 nm), and "car" (810 nm) with

false-color based on the $GaTe_{0.5}Se_{0.5}$-based image sensor. **c** Scanned grayscale images of "soil" (390 nm), "tree" (520 nm), and "river" (810 nm) and corresponding three-wavelength hybrid image based on the $GaTe_{0.5}Se_{0.5}$-based image sensor. **d** Noise power spectrum of the $GaTe_{0.5}Se_{0.5}$-based image sensor, measured under dark condition. **e** Polarization-sensitive photoresponse of the device within the wavelength range of 400-850 nm. **f** Demonstration of image convolutional processing operations, such as sharpness and edge extraction, utilizing the polarization-sensitive photoresponse under 450 nm laser illumination, compared to conventional convolution kernels.

Discussion

To summarize, we have successfully demonstrated image convolutional processing utilizing a $GaTe_{0.5}Se_{0.5}$-based polarization-sensitive photodetector, capable of configuring appropriate convolutional kernels through the utilization of polarized photoresponses. The $GaTe_{0.5}Se_{0.5}$-based photodetector exhibits polarization sensitivity across a wide-spectral photoresponse range (255 to 1064 nm), achieved via the incorporation of an artificially designed h-phase few-layered $GaTe_{0.5}Se_{0.5}$ semiconductor, which remains highly stable at room temperature through AIMD simulation, thus facilitating its application in wide-spectral imaging. Under 255, 390, 520, and 810 nm wavelengths illumination, the device has demonstrated its 2D imaging capability by leveraging the photodetector's photoresponse characteristics within the spectral range. Harnessing the polarization sensitivity of the device, the configuration of suitable convolutional kernels through polarized photoresponses allows for concurrent operations such as image sharpness and edge extraction on scanned images. In contrast to preceding methods, our approach exhibits considerable potential for advancing multifunctional optoelectronic devices, capable of addressing diverse and complex application scenarios, thus aligning with the trends towards integration and miniaturization. Furthermore, beyond the proof-of-concept demonstration presented in this study, further improvement of device structure and integration into device arrays will be imperative to drive this proposed concept toward practical applications.

Materials and methods

Crystal Growth and Characterization.

The $GaTe_{0.5}Se_{0.5}$ crystal was synthesized utilizing the chemical vapor transport (CVT) method. Liquid gallium (99.999%, Alpha), selenium powder (99.99%, Alpha), and tellurium powder (99.99%, Alpha) were employed as precursor substances in the chemical reaction. The above-mentioned substances were proportionally measured at a stoichiometric ratio of 2:1:1 and sealed in a quartz tube, which was subsequently evacuated to a vacuum state of approximately 10^{-3} Pa. In this process, trace amounts of iodine grains (99%, Alpha) were introduced as material transport agents without participating in the chemical reaction. The prepared vacuum quartz tube was placed in a dual-zone tube furnace, with the high-temperature zone set at 750°C and the low-temperature zone set at 600°C. The quartz tube was maintained in the furnace chamber at these temperature conditions for 5 days. Subsequently, the furnace chamber temperature was gradually cooled to 200°C at a rate of 10°C/h, followed by natural cooling of the chamber to room temperature.

The crystallographic structure, crystal quality, and fundamental properties of the $GaTe_{0.5}Se_{0.5}$ crystal synthesized via the aforementioned reaction were thoroughly investigated using a range of characterization techniques. These techniques included scanning transmission electron microscopy (STEM) equipped with energy-dispersive X-ray spectroscopy (EDS), Raman spectroscopy testing, photoluminescence (PL) testing, second harmonic generation (SHG) testing, and absorption testing. STEM characterization was conducted using a JEM-ARM200F atomic resolution analytical microscope. The bright-field imaging mode was selected for sample observation, and elemental mapping was employed to discern the positions of different atoms within the lattice, including Ga, Te, and Se. The cross-sectional sample was prepared using the FEI Scios2 dual-beam focused ion beam system. Raman spectroscopy and PL testing were performed using a microscopic confocal laser Raman spectrometer (InVia, Renishaw), excited by a 532 nm laser. SHG testing was carried out utilizing the MStarter 100 SHG Microspectral Scanning Test System and sample was excited by a

1064 nm laser, while absorption testing was conducted using the MStarter ABS DUV-NIR Microscopic Absorption Spectroscopy System. The differential transmission method was employed to characterize the samples by comparing the transmittance between the sample and the substrate.

Device Fabrication.

Multi-layered $GaTe_{0.5}Se_{0.5}$ nanosheets were obtained through a mechanical exfoliation method. The exfoliated nanosheets were then transferred onto SiO_2/Si substrates using polydimethylsiloxane (PDMS, PF-40/17-X4, purchased from Shanghai Onway Technology Co., Ltd). Back-gated field-effect transistors (BG-FETs) were fabricated, employing SiO_2 with a thickness of 300 nm as the dielectric layer and Si as the back gate. The source and drain electrodes of the devices were constructed using the channel-masking method, with gold (Au) chosen as the material for the source and drain electrodes, each with a thickness of 50 nm.

Electrical and optoelectrical measurements.

Electronic and optoelectronic measurements were conducted using an Agilent Technologies B1500A semiconductor device analyzer in conjunction with a homebuilt optoelectronic measurement platform. The response time of the device was determined using an oscilloscope (Rigol MSO5102) and an AOM (Acousto-Optic Modulator) Holy light modulator (Gooch & Housego 3080-125) incorporated into a proprietary optoelectronic measurement system. Spatial photocurrent mapping was performed using the Mstarter 200 High Precision Photocurrent Scanning Test Microscope. All measurements were carried out at room temperature and were repeated multiple times to ensure reproducibility.

Computational details.

The electronic band structure and optical properties of the bulk $GaTe_{0.5}Se_{0.5}$ was calculated by using the first-principle method of projector-augmented wave (PAW)[50] based on density functional theory (DFT) calculations, which were programmed in Vienna Ab initio Simulation Package (VASP)[51]. The generalized gradient approximation Perdew–Burke–Ernzerhof (GGA-PBE) of exchange and correlation functionals were used in the calculation[34, 52]. The band gaps and optical properties were

calculated with the HSE (Heyd−Scuseria−Ernzerhof) hybrid functional with a standard screening parameter of 0.2 (HSE06)[53]. The cut-off energy has been taken as 520 eV and the convergence tolerance force on each atom is taken up to 0.001 eV/Å using Gaussians smearing method for optimization of the structures. A Monkhorst–Pack k-mesh of $12 \times 12 \times 2$ sampling in the full Brillouin zone was used in calculations[54]. The van der Waals interactions was incorporated through the DFT-D3 approach[55]. The optical absorption coefficient $\alpha(\omega)$ was calculated from the dielectric function by using

$$\alpha(\omega) = \sqrt{2}\omega[\sqrt{\varepsilon_1^2(\omega) + \varepsilon_2^2(\omega)} - \varepsilon_1(\omega)]^{\frac{1}{2}}$$. Here, $\varepsilon_1(\omega)$ and $\varepsilon_1(\omega)$ are the real and imaginary part of complex dielectric function, respectively.

Data availability

The authors declare that the data supporting the findings of this study are available within the paper, Supplementary Information and Source Data are available from the corresponding authors upon request.

Author details

[1]State Key Laboratory of Superlattices and Microstructures, Institute of Semiconductors, Chinese Academy of Sciences, Beijing 100083, China. [2]Center of Materials Science and Optoelectronic Engineering, University of Chinese Academy of Sciences, Beijing 100049, China.

Author contributions

Z.W. supervised the project. Y.Y. conducted the sample growth, device fabrication, device measurement, and demonstration application. T.X., Y.-Y.L., and D.L. performed the theoretical calculations. Z. Z. performed the Raman spectrum measurement. Y.Y., J.H., and Z.W. wrote and revised the manuscript. All the authors discussed the experiments and commented on the manuscript.

Acknowledgements

Competing interests

References

1. Lythgoe, J., & Hemmings, C. Polarized Light and Underwater Vision. *Nature* **213**, 893–894 (1967).

2. Wan, L., Liu, Y., Fuchter, M. J. & Yan, B. Anomalous circularly polarized light emission in organic light-emitting diodes caused by orbital–momentum locking. *Nat. Photonics* **17**, 193-199 (2023).

3. Yao, F. et al. Measurement of complex optical susceptibility for individual carbon nanotubes by elliptically polarized light excitation. *Nat. Commun.* **9**, 3387 (2018).

4. Wei, J. et al. Geometric filterless photodetectors for mid-infrared spin light. *Nat. Photonics* **17**, 171-178 (2022).

5. Zhou, Z. et al. Low symmetric sub-wavelength array enhanced lensless polarization-sensitivity photodetector of germanium selenium. *Sci. bull.* **68**, 173-179 (2023).

6. Song, I. et al. Helical polymers for dissymmetric circularly polarized light imaging. *Nature* **617**, 92-99 (2023).

7. Tong, L. et al. Stable mid-infrared polarization imaging based on quasi-2D tellurium at room temperature. *Nat. Commun.* **11**, 2308 (2020).

8. Xu, Y., Yang, G., Xia, H., Zou, G., Zhang, Q. & Gao, J. Enantioselective synthesis of helical polydiacetylene by application of linearly polarized light and magnetic field. *Nat. Commun.* **5**, 5050 (2014).

9. Ge, B., Zhou, R., Takiguchi, Y., Yaqoob, Z. & So, P. T. C. Single-Shot Optical Anisotropy Imaging with Quantitative Polarization Interference Microscopy. *Laser Photonics Rev.* **12**, 1800070 (2018).

10. Rhee, H. et al. Femtosecond characterization of vibrational optical activity of chiral molecules. *Nature* **458**, 310-313 (2009).

11. Kim, S. K. et al. Tuning light absorption in core/shell silicon nanowire photovoltaic devices through morphological design. *Nano Lett.* **12**, 4971-4976 (2012).

12. Yeh, C.-H., Yang, Y.-C., Hsu, T.-A., Chen, Y.-W., Chow, C.-W. & Chen, J.-H. Adaptive and secure VCSEL FSO based on simple dual-polarized architecture for short distance transmission. *Phys. Scr.* **95**, 095505 (2020).

13. Chen, Y., Yang, X. & Gao, J. 3D Janus plasmonic helical nanoapertures for polarization-encrypted data storage. *Light Sci. Appl* **8**, 45 (2019).

14. Wang, X. et al. Polarimetric Image Sensor and Fermi Level Shifting Induced Multichannel Transition Based on 2D PdPS. *Adv. Mater.* **34**, e2107206 (2022).

15. Xu, P. et al. Polarized light source based on graphene-nanoribbon hybrid structure. *Opt.*

Commun. **395**, 76-81 (2017).

16. Sun, Z., Huang, Y., Bao, Y. & Wu, D. Polarized Remote Sensing: A Note on the Stokes Parameters Measurements From Natural and Man-Made Targets Using a Spectrometer. *IEEE Trans. Geosci. Remote Sens.* **55**, 4008-4021 (2017).

17. Wang, Z. et al. Strong In-Plane Anisotropic SiP_2 as a IV-V 2D Semiconductor for Polarized Photodetection. *ACS Nano* **15**, 20442-20452 (2021).

18. Wu, D. et al. In Situ Fabrication of $PdSe_2$/GaN Schottky Junction for Polarization-Sensitive Ultraviolet Photodetection with High Dichroic Ratio. *ACS Nano* **16**, 5545-5555 (2022).

19. Ahn, J. et al. Near-Infrared Self-Powered Linearly Polarized Photodetection and Digital Incoherent Holography Using WSe_2/$ReSe_2$ van der Waals Heterostructure. *ACS Nano* **15**, 17917-17925 (2021).

20. Wang, Y. et al. Applications of 2D-Layered Palladium Diselenide and Its van der Waals Heterostructures in Electronics and Optoelectronics. *Nanomicro Lett.* **13**, 143 (2021).

21. Pi, L. et al. Broadband convolutional processing using band-alignment-tunable heterostructures. *Nat. Electron.* **5**, 248-254 (2022).

22. Cho, H. et al. Real-time finger motion recognition using skin-conformable electronics. *Nat. Electron.* **6**, 619-629 (2023).

23. Lee, S., Peng, R., Wu, C. & Li, M. Programmable black phosphorus image sensor for broadband optoelectronic edge computing. *Nat. Commun.* **13**, 1485 (2022).

24. Feldmann, J. et al. Parallel convolutional processing using an integrated photonic tensor core. *Nature* **589**, 52-58 (2021).

25. Li, T. et al. Reconfigurable, non-volatile neuromorphic photovoltaics. *Nat. Nanotechnol.*, (2023). https://doi.org/10.1038/s41565-023-01446-8

26. Jang, H. et al. In-sensor optoelectronic computing using electrostatically doped silicon. *Nat. Electron.* **5**, 519-525 (2022).

27. Wu, S. et al. Ultra-sensitive polarization-resolved black phosphorus homojunction photodetector defined by ferroelectric domains. *Nat. Commun.* **13**, 3198 (2022).

28. Tian, R. et al. Chip-integrated van der Waals PN heterojunction photodetector with low dark current and high responsivity. *Light Sci. Appl* **11**, 101 (2022).

29. Wu, P. et al. Van der Waals two-color infrared photodetector. *Light Sci. Appl* **11**, 6 (2022).

30. Alonso, J. L., Andrade, X., Echenique, P., Falceto, F., Prada-Gracia, D. & Rubio, A. Efficient formalism for large-scale ab initio molecular dynamics based on time-dependent density functional theory. *Phys. Rev. Lett.* **101**, 096403 (2008).

31. Lü, J.-T., Leitherer, S., Papior, N. R. & Brandbyge, M. Ab initio current-induced molecular dynamics. *Phys. Rev. B* **101**, 201406(R) (2020).

32. G. Kresse, J. F. l. Efficient iterative schemes for ab initio total-energy calculations using a plane-wave basis set. *Phys. Rev. B* **54**, 11169-11186 (1996).

33. Kresse, G. & Furthmüller, J. Efficient iterative schemes for ab initio total-energy calculations using a plane-wave basis set. *Phys. Rev. B* **54**, 11169-11186 (1996).

34. Perdew, J. P., Burke, K. & Wang, Y. Generalized gradient approximation for the exchange-correlation hole of a many-electron system. *Phys. Rev. B* **54**, 16533-16539 (1996).

35. Lu, Y., Wang, H., Wang, L. & Yang, L. Mechanism of carrier doping induced magnetic phase transitions in two-dimensional materials. *Phys. Rev. B* **106**, 205403 (2022).

36. Muhimmah, L. C., Peng, Y.-H., Yu, F.-H. & Ho, C.-H. Near-infrared to red-light emission and

carrier dynamics in full series multilayer GaTe$_{1-x}$Se$_x$ (0≤x≤1) with structural evolution. *NPJ 2D Mater. Appl.* **7**, 3 (2023).

37. Muhimmah, L. C. & Ho, C.-H. Dual phase two-color emission observed in van der Waals GaTe planes. *Appl. Surf. Sci.* **542**, 148593 (2021).

38. Lei, S. et al. Synthesis and photoresponse of large GaSe atomic layers. *Nano Lett.* **13**, 2777-2781 (2013).

39. Hong, H. et al. Giant enhancement of optical nonlinearity in two-dimensional materials by multiphoton-excitation resonance energy transfer from quantum dots. *Nat. Photonics* **15**, 510-515 (2021).

40. Guo, Q. et al. Ultrathin quantum light source with van der Waals NbOCl$_2$ crystal. *Nature* **613**, 53-59 (2023).

41. Yu, Y. et al. Phase-Engineered Synthesis of Ultrathin Hexagonal and Monoclinic GaTe Flakes and Phase Transition Study. *Adv. Funct. Mater.* **29**, (2019).

42. He, W., Kong, L., Yu, P. & Yang, G. Record-High Work-Function p-Type CuBiP$_2$Se$_6$ Atomic Layers for High-Photoresponse van der Waals Vertical Heterostructure Phototransistor. *Adv. Mater.* **35**, e2209995 (2023).

43. Wang, R. et al. Controllable Inverse Photoconductance in Semiconducting Nanowire Films. *Adv. Mater.* **34**, e2204698 (2022).

44. Cui, Y. et al. Wavelength-selectivity polarization dependence of optical absorption and photoresponse in SnS nanosheets. *Nano Res.* **14**, 2224-2230 (2021).

45. Zhong, M. et al. Gate-controlled ambipolar transport in b-AsP crystals and their VIS-NIF photodetection. *Nanoscale* **13**, 10579-10586 (2021).

46. Bullock, J. et al. Polarization-resolved black phosphorus/molybdenum disulfide mid-wave infrared photodiodes with high detectivity at room temperature. *Nat. Photonics* **12**, 601-607 (2018).

47. Liang, Y. et al. Multilayered PdTe$_2$/GaN Heterostructures for Visible-Blind Deep-Ultraviolet Photodetection. *IEEE Electron Device Lett.* **42**, 1192-1195 (2021).

48. Wu, C. Y. et al. Non-Ultrawide Bandgap Semiconductor GaSe Nanobelts for Sensitive Deep Ultraviolet Light Photodetector Application. *Small* **18**, 2200594 (2022).

49. Peng, M. et al. Blackbody-sensitive room-temperature infrared photodetectors based on low-dimensional tellurium grown by chemical vapor deposition. *Sci. Adv.* **7**, eabf7358 (2021).

50. Blochl, P. E. Projector augmented-wave method. *Phys. Rev. B* **50**, 17953-17979 (1994).

51. Kresse, G. & Furthmuller, J. Efficient iterative schemes for ab initio total-energy calculations using a plane-wave basis set. *Phys. Rev. B* **54**, 11169-11186 (1996).

52. Perdew, J. P., Burke, K. & Ernzerhof, M. Generalized Gradient Approximation Made Simple. *Phys. Rev. Lett.* **77**, 3865-3868 (1996).

53. Heyd, J., Scuseria, G. E. & Ernzerhof, M. Hybrid functionals based on a screened Coulomb potential. *J. Chem. Phys.* **118**, 8207-8215 (2003).

54. Monkhorst, H. J. & Pack, J. D. Special points for Brillouin-zone integrations. *Phys. Rev. B* **13**, 5188-5192 (1976).

55. Grimme, S., Antony, J., Ehrlich, S. & Krieg, H. A consistent and accurate ab initio parametrization of density functional dispersion correction (DFT-D) for the 94 elements H-Pu. *J. Chem. Phys.* **132**, 154104 (2010).

Supplementary Files

This is a list of supplementary files associated with this preprint. Click to download.

- supportinginformation.docx